

# A Mechanostatistical Approach to Multiscale Computational Bone Remodelling



X. Wang and J. Fernandez

**Abstract** Computational models in biomechanics are generally unable to incorporate mechanical and anatomical data over the entire range of relevant spatial scales. This chapter proposes the construction of a framework, which unites several methodologies that operate on traditionally different aspects of bone remodelling, bridging the gap between previously incompatible data. The presented framework is used to solve the load adaptation response of the femoral neck as an application and consists of passing data from different sources across a multitude of spatial scales to solve for both organ-level and Haversian-level biomechanical states. The solutions are then stored in a database, to be utilised by a statistical method which can quickly estimate new load adaptation responses for which solutions were not previously generated, cutting down computation time.

## 1 Introduction

Bone damage and fracture from osteoporosis remain a costly medical condition with significant implications for the quality of life among those who have suffered injuries. For this reason, much research has been devoted to the understanding, treatment, and prevention of bone-related diseases, especially among the elderly. Currently, the widely known mechanobiological model of Wolff's law of bone adaptation and its successor, the *mechanostat* of the Utah Paradigm [1], still holds great explanatory power for its conceptual simplicity and remains a core component to the many existing computational bone adaptation models primarily informed by biomechanics.

---

X. Wang (✉)

Auckland Bioengineering Institute, 70 Symonds St, Auckland, New Zealand  
e-mail: [xm.wang@auckland.ac.nz](mailto:xm.wang@auckland.ac.nz)

J. Fernandez

Department of Engineering Science, Auckland Bioengineering Institute, 70 Symonds St, Auckland, New Zealand  
e-mail: [j.fernandez@auckland.ac.nz](mailto:j.fernandez@auckland.ac.nz)

© Springer Nature Switzerland AG 2020

J. Belinha et al. (eds.), *The Computational Mechanics of Bone Tissue*,  
Lecture Notes in Computational Vision and Biomechanics 35,  
[https://doi.org/10.1007/978-3-030-37541-6\\_6](https://doi.org/10.1007/978-3-030-37541-6_6)

Although there is a wealth of literature on the topic, most attempts at constructing an *in silico* model for bone remodelling are immediately confronted with three competing factors, which limit the available computational resources for a feasible evaluation. These are: (i) the geometric detail; (ii) the spatiotemporal scale; and (iii) the applied constitutive mechanical laws. The existing studies have attempted to balance the amount of detail considered for each of these factors. Fernandez [2] and McNamara [3] have demonstrated bone remodelling behaviour in two dimensions at the microscale in cortical and trabecular bone, respectively, complete with changes in microgeometry; the model given by Fernandez has further demonstrated the merging of pores as an emulation of osteoporosis, while the study by McNamara has explored various modes of damage and recovery in the calculation of bone adaptation. Beaupre et al. [4] constructed a model which simulates the bone density changes of a long-term load response of a 2D macrolevel model to external loads, providing a foundation for models investigating the response to sustained exercise regimes. Coelho et al. [5] introduced a 3D multiscale hierarchical approach, characterising bone spatial variation with repeating microstructures in several discrete regions. Other important aspects of computational bone remodelling have produced studies focussing on modelling osteoclast biochemistry [6], bone resorption and stress shielding from orthopaedic implants [7], and reduction of solution time with neural network approaches [8].

Apart from the difficulty of capturing complex geometries and scales, most existing literature disproportionately focus on trabecular bone remodelling when the cortical to trabecular loading ratio is estimated to be as high as 65:35 [9].

This chapter proposes the development of a multiscale modelling framework within the context of hip fracture for the swift prediction of bone strain and the estimation of its adaptation response for a given exercise regime. The development of the framework is divided into three parts: Part I utilises finite elements (FE) to solve for the mechanical state of bones at the macroscale; Part II incorporates a collection of algorithms based on a previous study [10], which addresses microscale Haversian-level bone adaptation in response to loading based on ideas from the mechanostat; and Part III describes a statistical surrogate model using partial least squares regression (PLSR), which addresses the problem of computation time. The integration of multiscale information allows the framework to remain anatomically and physiologically relevant at all spatial scales and features high compatibility with clinically important measurements and biomechanical data.

In Part I, we describe the construction of a biomechanical model from the visible human (VH) data set of muscles and bones in the hip area and subject it to loading obtained from gait analyses, from which we obtain stresses at the femoral neck cortical bone. This femoral neck cortex henceforth will be referred to as the framework's region of interest (ROI). In Part II, we summarise the construction of Haversian-scale FE models and link the ROI with the set of Haversian models through the propagation of stresses from the macroscale down to the microscale. Furthermore, we describe two load transduction algorithms, which affect cortical bone at the Haversian scale;

the first alters localised bone strength via a change in bone mineral density, and the second alters Haversian microstructure. When combined, these algorithms form our approach to bone remodelling and load adaptation. In Part III, we detail the construction of a database of stress scenarios and resulting homogenised material properties and utilise PLSR to predict the evolution of material properties given non-simulated load cases.

All FE simulations utilised the software package SIMULIA Abaqus ([www.3ds.com](http://www.3ds.com)). A schematic of the framework and its information sources is shown in Fig. 1. The framework is categorised into two phases: the construction phase details the process behind building each part of the framework, and the application phase is where the framework is used for solving the load adaptation problem. The large savings in computation time occur due to the replacement of Part II in the framework construction phase, the *adaptation response*, with Part II in the framework application phase, the *response database*.

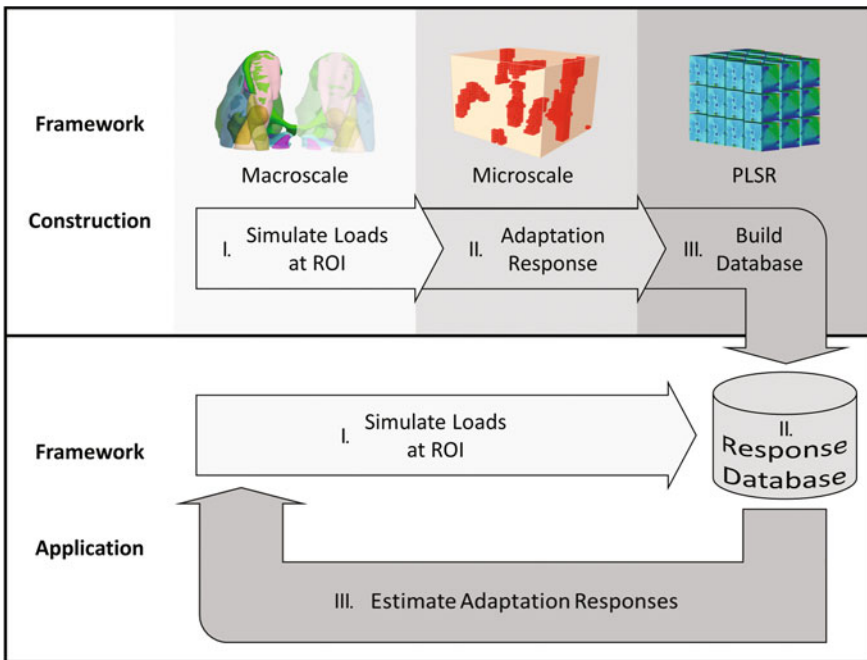


**Fig. 1** Framework diagram. Shades refer to the different parts of the framework. (Light grey) Part I, collection of load information from macroscale; (grey) Part II, receiving load information from Part I and formulating the adaptation response which takes the form of homogenised material properties; (dark grey) Part III, statistical model of responses

## 2 Part I: Macroscale FE Model

### 2.1 Model Construction

Bone and muscle shapes were extracted and meshed with hexahedral 2 mm reduced integration elements from the VH data set [11] from 269 colour photograph slices in the original resolution of  $0.33 \text{ mm} \times 0.33 \text{ mm}$  per pixel and 1 mm of spacing between slices.

Anatomically realistic porosity variations  $P^e = \{p_i^e\}$ ,  $1 \leq i \leq n^e$ , with  $n^e$  as the total number of ROI elements, were statistically generated from Gaussian distributions based on experimentally determined values and uncertainties for circumferentially varying femoral cortex porosities [12]. The generated porosities for the femoral cortex elements provide a realistic femoral neck mesh on which FE mechanics simulations are run.

### 2.2 Mechanical Simulations

The simulation consists of two sections:

1. Initialisation, which estimates key parameters under the prescribed initial conditions and
2. Progression, which emulates the evolution of the bone state.

#### 2.2.1 Macroscale Initialisation

Bones were subjected to muscle forces recorded from walking gait analysis [13] with simulation under linear elasticity and isotropic material properties shown in Table 1.

Maximum absolute principal stresses  $S^e = \{s_i^e\}$ ,  $1 \leq i \leq n^e$  for each element were recorded at the ROI element integration points as the load transduction signal for Haversian modelling. To incorporate the observation that bone fibres align in a direction, which maximally resists stresses and strains, fibre directions were estimated from the eigenvalue decomposition of the stress tensors from FE load simulations, as shown in Fig. 2.

#### 2.2.2 Macroscale Progression

The evolution of the mechanical state of the femoral cortex was simulated for a total of  $T = 90$  days of simulation time, with iteration steps of one day. In each iteration,  $S^e$  is passed to the PLSR model in Part III, which outputs a set of evolved homogenised

**Table 1** Macroscale anatomical structures and their respective material properties as applied in FE simulations

Structure	Category	$E$ (GPa)	$\nu$	Notes
Adductor brevis, longus, magnus Biceps femoris Gluteus maximus, medius, minimus Gracilis Iliacus Rectus femoris Sartorius Semitendinosus	Muscle	0.27	0.4999	$E$ from [15]; $\nu$ from [16]
Hip bone	Cortical	14.65	0.332	[17]
Femur <sup>a</sup>	Cortical	14.65	0.332	Not ROI for $t > 0^b$ ; [18] Femoral head <sup>c</sup> ; [19] Cancellous bone <sup>d</sup>
	Cartilage	0.580	0.39	
	Trabecular	3.386	0.12	

All are modelled as isotropic elastic materials

<sup>a</sup>Femur is composed of three different types of materials

<sup>b</sup>ROI material properties evolve after the initialisation step ( $t = 0$ ). Rest of the cortex does not change

<sup>c</sup>Femoral head is modelled with a layer of cartilage surrounding the cortex

<sup>d</sup>Femur is modelled with a thick layer of cortex elements and filled with trabecular elements

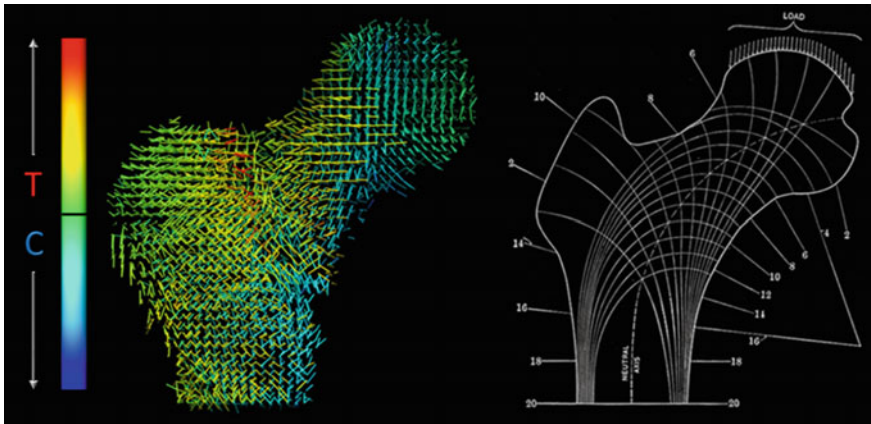


**Fig. 2** Left: stress tensor eigendecomposition of internal simulated stresses of the proximal femur at the trabecular bone. Colour and line direction indicates magnitude and direction of maximum absolute eigenvalue and eigenvector, respectively; with reference to the colour bar, green to blue colouration indicates a compressive minimum principal stress (C), and green to red colouration indicates a tensile maximum principal stress (T). Eigenvectors match closely with stress lines found in other studies of bone stress, e.g. Koch’s mathematical analysis. Right: adapted from Gray [14]; note the compressive stresses running in the proximal-distal direction along the medial shaft through the femoral head, and the tensile stresses running up the lateral shaft then in the direction of the femoral neck axis. The criss-cross pattern through the core indicates the co-dominance of both tensile and compressive stress directions and closely resembles trabecular anatomy (see Fig. 7)

material properties as a result of the construction of a database of material property evolutions built in Part II.

### 3 Part II: Microscale Haversian Model

#### 3.1 Model Construction

Haversian anatomy was constructed and voxel meshed with  $5\ \mu\text{m}$  elements from microcomputed tomography ( $\mu\text{CT}$ ) images (Table 2) at  $5\ \mu\text{m}$  resolution of an equine cortical bone biopsy of dimensions  $4\ \text{mm} \times 3.5\ \text{mm} \times 2\ \text{mm}$  (Fig. 3, left). The use of equine data was justified in our framework as (i) equine models are highly translational to human contexts due to similar Haversian anatomy and have been

**Table 2** Micro-CT imaging parameters

X-ray energy	60 kV, 10 W
Exposure time for each projection	60 s
Total number of projections	721
Objective magnification	4 $\times$
Source to sample distance	120 mm
Detector to sample distance	40 mm
Pixel numbers	1024 $\times$ 1024 $\times$ 1024
Effective voxel size	5 $\mu\text{m}$

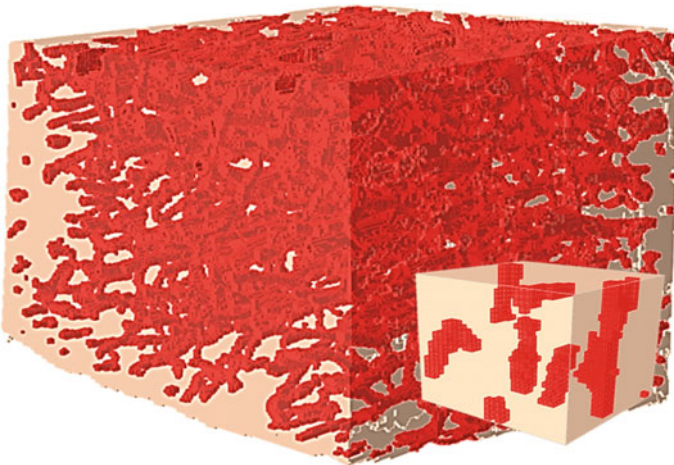


**Fig. 3** Left: equine biopsy mesh showing Haversian canals. Right: example Haversian representative mesh cut from the biopsy mesh (not to scale)

recommended by the US Federal Drugs Administration (FDA) for comparative joint research [20], and (ii) there exists in vivo bone strain and biomarker data from equine studies, unlike human data which only reports post-mortem information. A database of Haversian models was formed from cutting  $n^m = 4$  samples of on average  $0.003 \text{ mm}^3$  from the voxel mesh, chosen as a size which contains a representative number of Haversian canals for microscale anatomy and material strength changes to be observed (Fig. 3, right). These samples were chosen based on their volume fraction of canal elements versus dense cortical bone elements, and thus contained porosity information to be matched to the porosity variation generated in Part I, obtained as

$$P^m = \{p_j^m\}, \quad 1 \leq j \leq n^m \quad (1)$$

### 3.2 Macro-microscale Link

#### 3.2.1 Haversian Link to ROI Elements

For each ROI element  $i$  and associated porosity  $p_i^c$ , lower and upper bounding porosities  $p_i^{m\alpha}$  and  $p_i^{m\beta}$  were extracted from  $P^m$ . Subsequently, the link from the ROI elements to the Haversian models is defined by weights  $w_i^\alpha$  and  $w_i^\beta$ :

$$w_i^\alpha = \begin{cases} \frac{p_i^{m\beta} - p_i^c}{p_i^{m\beta} - p_i^{m\alpha}}, & p_i^{m\alpha} < p_i^c < p_i^{m\beta} \\ \frac{1}{2}, & p_i^{m\alpha} = p_i^c = p_i^{m\beta} \end{cases}$$

$$w_i^\beta = \begin{cases} \frac{p_i^c - p_i^{m\alpha}}{p_i^{m\beta} - p_i^{m\alpha}}, & p_i^{m\alpha} < p_i^c < p_i^{m\beta} \\ \frac{1}{2}, & p_i^{m\alpha} = p_i^c = p_i^{m\beta} \end{cases} \quad (2)$$

This allows any parameter of the  $i$ th ROI element to be represented by a weighted sum of its corresponding parameters of the linked Haversian models.

#### 3.2.2 Stress Propagation from ROI to Haversian Models

The local positive  $z$  directions for each Haversian model were defined to be parallel to the fibre directions estimated from the elements in the ROI. To determine the appropriate load range for each Haversian model  $j$  from the propagation, we formulate sets of reverse links by constructing a set of ROI element indices, which is associated with these elements:

$$I_j^m = \left\{ i : p_j^m \in \left\{ p_i^{m\alpha}, p_i^{m\beta} \right\} \right\}, \quad 1 \leq i \leq n^e \quad (3)$$

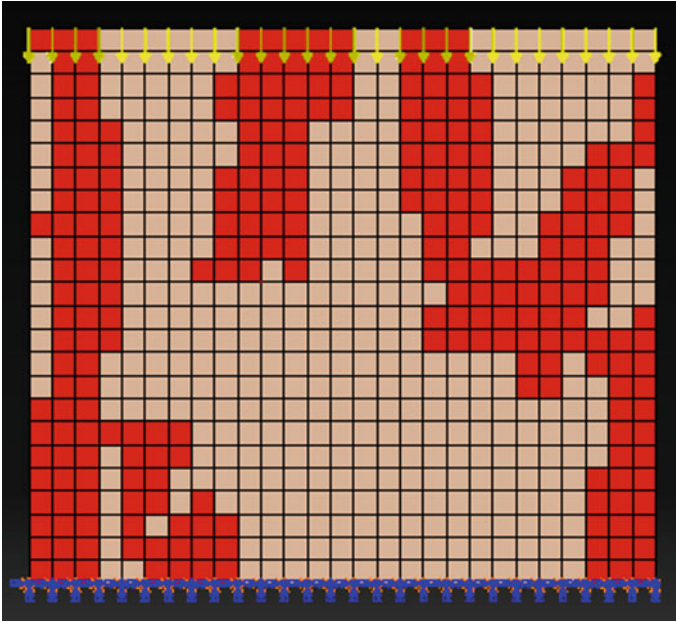


**Fig. 4** Side view of application of load on a Haversian specimen. Blue symbols (bottom) indicate spatial and rotational fixed boundary conditions. Yellow arrows (top) indicate load direction

Taking the magnitude  $s_i$  of the maximum absolute principal stress on the ROI element centroid as the most significant component of the load, we calculate a set of loads  $L_j$  which appear in the macroscale initialisation step (Sect. 2.2.1) as

$$L_j = \frac{s_i}{a_j}, \quad i \in I_j^m \quad (4)$$

where  $a_j$  is the surface area of the load application. An example of a typical loading scenario of a Haversian specimen is given in Fig. 4.

### 3.3 Haversian Simulation

#### 3.3.1 Microscale Initialisation

For each Haversian model  $j$ , the models were simulated under five different evenly spaced loading regimes between  $\min(L_j)$  to  $\max(L_j)$  under linear elasticity with isotropic elements. An isotropic Young's modulus was assigned to the cortical elements based on the homogenised cortical and canal values and the fraction of cortical and canal elements in the model (see Table 3).



**Table 3** Microscale model parameters

Name/description	Parameter values	Notes
Cortical $\nu$	0.3	Cortical $E$ varies with $P^m$
Canal $E$	2 MPa	
Canal $\nu$	0.167	
Canal $\rho$	1 kg mm <sup>-3</sup>	Same as water
$c_1$	4621.36 MPa	From Eq. (7) parameters at $t = 0$
$c_2$	1.075 kg m <sup>-3</sup> s <sup>-1</sup>	Remodelling constant; from [2]
$b$	1.54	Power law exponent; from [21]
Canal closing rate	1.9 nm s <sup>-1</sup>	Adapted from canine data in [22]
Canal opening rate	2.083 nm s <sup>-1</sup>	From [6]
$L^I$	-500 $\mu\epsilon$	Adapted from [2]
$L^{II}$	+500 $\mu\epsilon$	
$L^{III}$	+2000 $\mu\epsilon$	

### Formulation of the Mechanostat

The initial simulations allowed the determination of the model's elementwise mechanostat across Haversian models  $j$  and their corresponding cortical elements  $k$ , defined by the piecewise density evolution parameter

$$\varepsilon_{jkt} = \begin{cases} \varepsilon_{jkt}^{\text{VMS}} - L_{jkt}^I, & \varepsilon_{jkt}^{\text{VMS}} < L_{jkt}^I \\ 0, & L_{jkt}^I \leq \varepsilon_{jkt}^{\text{VMS}} < L_{jkt}^{II} \\ \varepsilon_{jkt}^{\text{VMS}} - L_{jkt}^{II}, & L_{jkt}^{II} \leq \varepsilon_{jkt}^{\text{VMS}} < L_{jkt}^{III} \\ L_{jkt}^{III} - \varepsilon_{jkt}^{\text{VMS}}, & \varepsilon_{jkt}^{\text{VMS}} \geq L_{jkt}^{III} \end{cases} \quad (5)$$

where  $\varepsilon_{jkt}^{\text{VMS}}$  is the von Mises stimulus strain at time step  $t$ .

The four conditions governing the piecewise function determine the four *zones* of the mechanostat (Fig. 5), where the region below  $L^I$  is the resorption zone which encourages bone resorption due to lack of loading, the region between  $L^I$  and  $L^{II}$  is the adapted state (homeostatic) zone where no changes occur, the region between  $L^{II}$  and  $L^{III}$  is the growth zone which encourages an increase in bone mineral density, and the region above  $L^{III}$  is the failure zone which also causes bone resorption. In the initialisation step ( $t = 0$ ), where the strain stimulus is defined to be in the centre of the adapted state zone, the piecewise function's boundaries are given by

$$\begin{aligned} L_{jk0}^I &= \varepsilon_{jk0}^{\text{VMS}} + L^I \\ L_{jk0}^{II} &= \varepsilon_{jk0}^{\text{VMS}} + L^{II} \end{aligned}$$

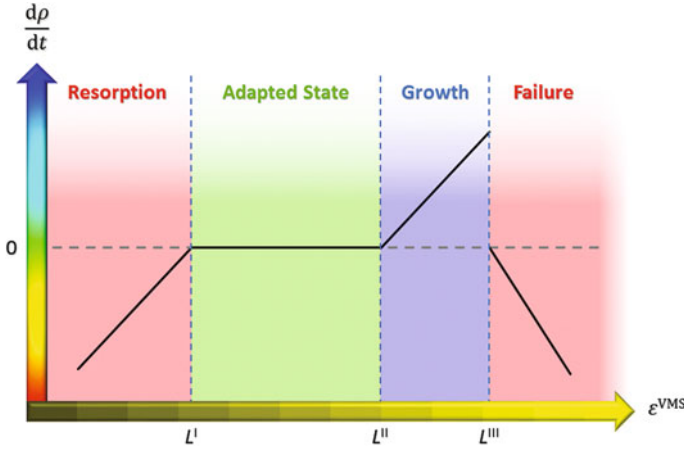


**Fig. 5** Illustration of the zones of the mechanostat, indicating the rate of change of bone density as a function of strain

$$L_{jk0}^{\text{III}} = \varepsilon_{jk0}^{\text{VMS}} + L^{\text{III}} \quad (6)$$

### Initialisation of Element-wise Density

The elementwise material properties also allowed the determination of an initial elementwise density  $\rho_{jk0}$  through a power law relation [21], given by

$$E_{jkt} = c_1 \rho_{jkt}^b \quad (7)$$

where  $E_{jkt}$  at  $t = 0$  is the initial Young's modulus.

### 3.3.2 Microscale Progression

The Haversian models were simulated for a total of  $T = 90$  days, with iteration steps of one day. Each Haversian model  $j$  across the five initial loads was subjected to three different evenly spaced excitation loads between values from  $0.375 \times \min(L_j)$  to  $1.5625 \times \max(L_j)$  across its loading surface. Each excitation load was further applied at seven evenly spaced angles between  $0^\circ$  and  $90^\circ$ . The strain state of the model was obtained after each iteration, where for each Haversian cortical element the von Mises stimulus  $\varepsilon_{jkt}^{\text{VMS}}$  was calculated from the strain tensor.

### Calculation of the Strain Stimulus

The data given in Table 4 shows that bone growth continues in the rest period after the exercise regime has ceased, indicating that the strain stimulus does not immediately revert back to pre-exercise levels. The von Mises strain stimulus  $\varepsilon_{jkt}^{\text{VMS}}$  in Eq. (5) is thus formulated as a weighted moving average on the actual von Mises equivalent

**Table 4** Cortical bone growth rates in horse specimens determined from oxytetracycline/fluorescein complexone staining in a histological sample taken from the dorsal cortex in equine third metacarpal bone, from Davies [23]

Days	Growth rate per day, $\mu\text{m} \pm \text{SD}$		Significance ( $p$ -value), control versus exercised
	Control	Exercised	
40	$1.8 \pm 1.1$	$2.6 \pm 2.6$ (Trot)	0.510
40	$3.2 \pm 4.3$	$2.2 \pm 3.3$ (Canter)	0.680
40	$2.1 \pm 2.9$	$12.7 \pm 8.6$ (Gallop)	0.017
40	$1.2 \pm 0.7$	$4.3 \pm 2.5$ (Rest)	0.014

strain  $\varepsilon_{jkt}^{\text{VM}}$ . The von Mises equivalent strain is used to determine  $\varepsilon_{jkt}^{\text{VMS}}$  by

$$\varepsilon_{jkt}^{\text{VMS}} = \sum_{\tau=1}^{\tau_{\max}} U(\tau) H_{jk}(\tau) \tag{8}$$

where  $\tau_{\max} = 30$  and  $U(\tau)$  and  $H_{jk}(\tau)$  are sets of weights and historical von Mises strains, respectively, given by

$$\begin{aligned} T^{\text{W}} &= \{1, 2, \dots, \tau_{\max}\} \\ M^{\text{W}} &= \{t + \tau - \tau_{\max}\}, \quad \tau \in T^{\text{W}} \\ U' &= \{\exp(\tau - \tau_{\max})\}, \quad \tau \in T^{\text{W}} \\ U &= \frac{U'}{\sum U'} \\ H_{jk} &= \{\varepsilon_{jk\mu}^{\text{VM}}\}, \quad \mu \in M^{\text{W}} \end{aligned} \tag{9}$$

Here, exp is the exponential function and  $\sum U = 1$ . The mechanostat boundaries from Eq. (6) shift by an amount equal to the difference between the current and previous stimulus strains:

$$\begin{aligned} L_{jkt}^{\text{I}} &= L_{jk,t-1}^{\text{I}} + \varepsilon_{jkt}^{\text{VMS}} - \varepsilon_{jk,t-1}^{\text{VMS}} \\ L_{jkt}^{\text{II}} &= L_{jk,t-1}^{\text{II}} + \varepsilon_{jkt}^{\text{VMS}} - \varepsilon_{jk,t-1}^{\text{VMS}} \\ L_{jkt}^{\text{III}} &= L_{jk,t-1}^{\text{III}} + \varepsilon_{jkt}^{\text{VMS}} - \varepsilon_{jk,t-1}^{\text{VMS}} \end{aligned} \tag{10}$$

The von Mises equivalent strain is used as the stimulus criteria as it considers both normal and shear deformations. This is formulated as

$$\varepsilon^{\text{VM}} = \frac{\sqrt{(\varepsilon_{11} - \varepsilon_{22})^2 + (\varepsilon_{22} - \varepsilon_{33})^2 + (\varepsilon_{33} - \varepsilon_{11})^2 + 6(\varepsilon_{12}^2 + \varepsilon_{23}^2 + \varepsilon_{31}^2)}}{\sqrt{2}(1 + \nu')} \tag{11}$$

with the strain components  $\varepsilon_{qr}$  as that found from the strain tensor  $\varepsilon_{jkt}$ , and  $\nu'$  is the equivalent Poisson's ratio, which is equal to the material Poisson's ratio  $\nu$  under elastic constitutive laws.

### Density and Young's Modulus Evolution

The density evolution parameter  $\varepsilon_{jkt}$  is calculated from Eq. (5). This causes a change in the density according to the forward Euler formulation

$$\rho_{jkt} = \rho_{jk,t-1} + c_2 \varepsilon_{jkt} \quad (12)$$

The updated density is subsequently converted to a Young's modulus via Eq. (7).

### Haversian Microstructure Evolution

Haversian microstructure changes according to osteoclast and osteoblast activity at the head and tail, respectively, of Haversian canals; bone resorption and deposition occur at the head and tail, and the regions where these activities occur are known as the *cutting* and *closing* regions.

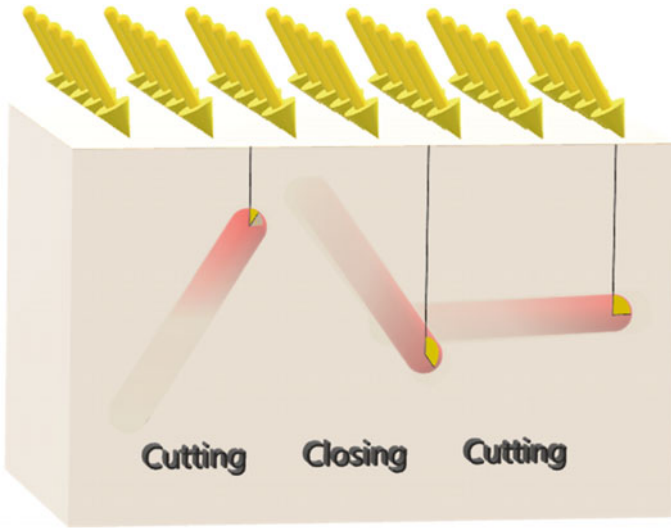
TIFF image stacks were generated from the element states of the Haversian model. With each element represented as a pixel, black and white binary colour values were assigned to the cortical and canal elements, respectively. The image stacks were subsequently passed to Fiji (fiji.sc/Fiji) for morphological thinning via medial axis skeletonisation (Skeletonize3D plugin, fiji.sc/Skeletonize3D) and a shape analysis on the generated skeleton (fiji.sc/AnalyzeSkeleton). This analysis allowed the determination of the cutting and closing regions of the canal and their present evolution directions.

Figure 6 shows the guidelines behind the determination of cutting and closing regions, with respective rates of  $2.083 \text{ nm s}^{-1}$  and  $1.9 \text{ nm s}^{-1}$  as given in Table 3. For all canal ends which are classified as cutting, the cutting direction  $\mathbf{g}$  was determined by

$$\mathbf{g} = \sum_{\gamma=1}^{n^l} \mathbf{V}_{\gamma}^T \boldsymbol{\lambda}_{\gamma} \quad (13)$$

where T is the matrix transpose operation,  $n^l$  is the number of cortical elements at the boundary between the cutting region and the canal elements, and  $\mathbf{V}_{\gamma}$ ,  $\boldsymbol{\lambda}_{\gamma}$  are a horizontally concatenated matrix of eigenvectors and a vector of eigenvalues, respectively, found through the eigendecomposition of the strain tensor  $\boldsymbol{\varepsilon}_{j\gamma t}$ . The direction  $\mathbf{g}$  typically aligns with the longitudinal direction in cortical bone towards the zones of highest strain and is heavily influenced by the angle of load application, as shown in Fig. 7.

Elements undergoing resorption receive canal material properties as specified in Table 3, and elements which have been mineralised by the closing cone receive material properties equal to the average of the surrounding cortical elements in the closing regions.



**Fig. 6** Determination of Haversian canal activity type based on canal geometry and load application. The type of activity that the Haversian canal undergoes is determined through the angle between the current canal direction and the closest point of load application. An acute or right angle categorises the canal end as a cutting cone, while an obtuse angle categorises the canal end as a closing cone

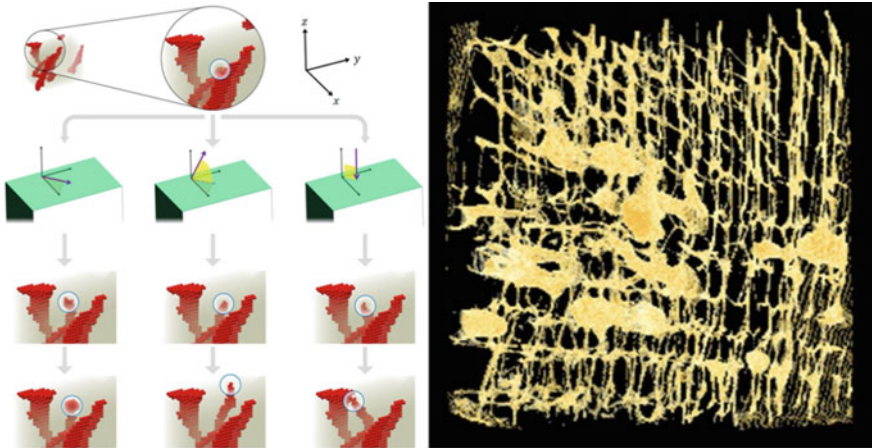


**Fig. 7** Comparison between simulated canal evolution and anatomical morphology. Left: example of the change in canal evolution due to different load angle applications (purple) along the surface (green) in the first row. Red pie sectors specify the angular deviation from the  $x$ -axis, and yellow pie sectors indicate the angular deviation from the  $xy$  plane. A single Haversian model was subjected to three different loading angles of the same magnitude; the region in the solid blue circle shows a cutting cone. Left column: pure shear load  $45^\circ$  from the  $x$ -axis; middle column: tensile load  $45^\circ$  from the  $x$ -axis and  $67.5^\circ$  from the  $xy$  plane; right column: pure normal compressive load to the  $xy$  plane. Compare tunnelling behaviour with example (right) of equine Haversian canals reconstructed from  $\mu$ CT data and estimated trabecular fibre directions in Fig. 2. Adapted from Wang et al. [10] with permission from Springer Nature

## 4 Part III: Statistical Modelling Using PLSR

### 4.1 Database Construction

Partial least squares regression [24] is used to relate two sets of matrices, the sample predictors  $X$  and corresponding sample responses  $Y$ , of data via a linear multivariate model, with the capability of analysing non-independent and incomplete variables in either matrix. Once the model has been trained on  $X$  and  $Y$ , it can be utilised to compute new responses from predictors which were not in the training sample.

The database is constructed on 420 Haversian simulations, consisting of all parameter combinations of the four porosities, five initial loads, three excitation loads, and seven application angles, with the addition of the time iteration step of each simulation. The values of these parameters in each combination form  $X$  for a total of 3780 parameter combinations.

The response  $Y$  is chosen as the homogenised Young’s modulus  $E_{jt}^H$  as a result of the Haversian simulations. This is given by

$$E_{jt}^H = \frac{1}{n^e} \sum_k E_{jkt} \tag{14}$$

The error in the PLSR response predictions was evaluated using a leave-one-out analysis, where each of the 3780 predictor/response sets was left out of the training data set and predicted using the rest of the training data. This is repeated for each set. Table 5 shows results from two samples of Haversian models for a time iteration at 30 days which indicate that homogenised Young’s modulus was predicted with less than 0.4 and 0.2% error, respectively.

**Table 5** Error of PLSR predictions for homogenised Young’s modulus in two different specimens, varying load angle and magnitude

Excitation magnitude <sup>a</sup>	Angle from <i>xy</i> plane (degrees)						
	0	15	30	45	60	75	90
<i>Specimen 1</i>							
0.375	0.02	0.06	<0.01	<0.01	0.03	0.06	0.25
1	0.50	0.12	0.13	0.21	0.15	0.12	0.30
1.5625	0.15	0.37	0.24	0.09	0.05	0.42	0.16
<i>Specimen 2</i>							
0.375	0.08	0.57	0.19	0.05	0.04	0.38	0.21
1	0.13	0.22	0.08	0.16	0.25	0.11	0.06
1.5625	0.16	0.04	0.36	0.02	0.16	0.03	0.07

<sup>a</sup>Excitation load magnitude is given as a factor of the initial magnitude

## 4.2 Macroscale-PLSR Link

The index link from the ROI elements to the Haversian models is retrieved as the weights from Eq. (2). For each iteration of the femoral cortex mechanical state, the homogenised material properties  $E_{it}^H$  for the  $i$ th ROI element are updated as

$$E_{it}^H = w_i^\alpha E_i^{P\alpha} + w_i^\beta E_i^{P\beta} \quad (15)$$

where  $E^P$  is the PLSR response function for the homogenised Young's modulus and

$$\begin{aligned} E_i^{P\alpha} &= E^P(p_i^{m\alpha}, l^0, l^x, \vartheta) \\ E_i^{P\beta} &= E^P(p_i^{m\beta}, l^0, l^x, \vartheta) \end{aligned} \quad (16)$$

with  $l^0$ ,  $l^x$ , and  $\vartheta$  as the initial load, excitation load, and angle of the excitation load, respectively.

## 4.3 Example Prediction

Figure 8 shows the strains simulated from the right femur ROI to material property changes predicted from PLSR, stimulated by walking and running exercises. The femur was originally conditioned to a walking exercise regime and subsequently subjected to the same walking exercise or changed to a running exercise regime for 90 simulated days, and PLSR was used to predict the Young's modulus at days 50 and 90. The effect of the adaptation is shown by the change in von Mises strains since day 1 when subjected to the same exercises since day 1.

The von Mises strains from the running exercises effected higher remodelling stimuli than the walking stimulus, as seen in the top row at  $t = 1$ . This is reflected in the strain response, where the walking exercise shows smaller strain changes than the running exercise. The former corresponds to much of the ROI falling in the adapted state zone in Fig. 5, while growth and failure regions are more abundant in the running series and appear earlier as seen in the strain changes at  $t = 50$  and  $t = 90$ .

Large regions of high strains are found at the posterior lateral region of the femoral neck cortex, while more moderately high strains are found at the anterior lateral region, agreeing with calculations of femoral neck cortical strains from hip muscle contractions [25]. The higher strains at the posterior lateral region correspond to bone weakening and the mechanostat failure zone, with large zones of bone weakening appearing in the running series and smaller, and moderate amounts of weakening appearing in the walking series. In contrast, the large regions of moderately high strains appearing at the anterior lateral region corresponded to a growth response in the running series and little to no response in the walking series.

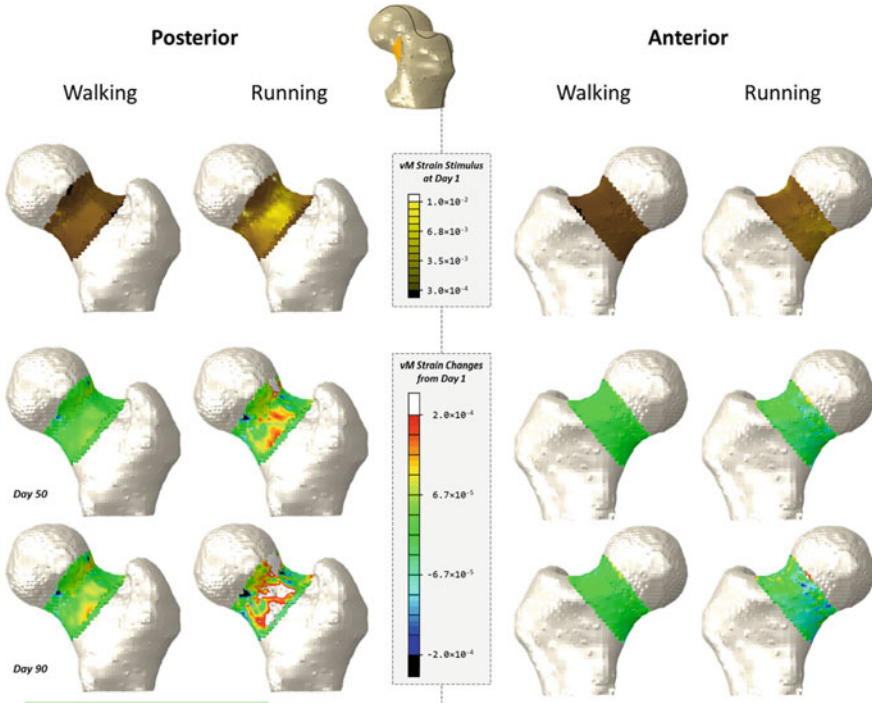


**Fig. 8** Von Mises strain changes due to PLSR-predicted homogenised Young's moduli from different exercise regimes over 90 simulated days. With reference to Fig. 5, strengthening is shown through negative strain changes, corresponding to the growth zone of the mechanostat, while weakening is shown through positive strain changes, corresponding to the failure zone. Stable areas with little to no strain changes fall in the adapted state zone

From these results, the PLSR is shown to be able to capture spatially varying patterns of bone growth and resorption as governed by the mechanostat. Adapted state regions are generally more widespread in the walking series, and the running series exhibited bone strengthening in moderately high strain regions and bone weakening in extremely high strain regions.

## 5 Conclusions

The presented work in this chapter proposes a framework incorporating detailed anatomical and biomechanical data across all relevant spatial scales to solve for the strain state and estimate an adaptation response for given stresses obtained from bone exercise regimes. In particular, the adaptation response is modelled at the microscale and the effects emerge at the macroscale, reflecting in vivo bone density changes at the Haversian level. We demonstrate that it is possible to circumvent lengthy computation



times and mitigate the loss of important detail through the application of statistical techniques, namely a partial least squares regression in this case, resulting in rapid prediction of the state of strains and bone strength from given exercise regimes. The presented techniques may be adapted to other bone joints to make use of the rich information available at different spatial scales. For example, in this study, we used information from high-resolution  $\mu$ CT of Haversian canals and biomarker data showing rates of bone turnover from equine models to inform macroscale responses. This modelling pipeline exhibits strong relations between changes observed at Haversian levels and the homogenised whole bone response, linking microscale adaptation with functional behaviour such as walking and running measured at the whole organ level. Outside of standard functional behaviour, the pipeline has the potential to explore disease states at the Haversian microscale and how these states manifest as changes at larger scales.

## References

1. Frost HM (2000) The Utah paradigm of skeletal physiology: an overview of its insights for bone, cartilage and collagenous tissue organs. *J Bone Miner Metab* 18(6):305–316
2. Fernandez JW, Das R, Cleary PW, Hunter PJ, Thomas CD, Clement JG (2013) Using smooth particle hydrodynamics to investigate femoral cortical bone remodelling at the Haversian level. *Int J Numer Methods Biomed Eng* 29(1):129–143. <https://doi.org/10.1002/cnm.2503>
3. McNamara LM, Prendergast PJ (2007) Bone remodelling algorithms incorporating both strain and microdamage stimuli. *J Biomech* 40(6):1381–1391. <https://doi.org/10.1016/j.jbiomech.2006.05.007>
4. Beaupre GS, Orr TE, Carter DR (1990) An approach for time-dependent bone modeling and remodeling-application: a preliminary remodeling simulation. *J Orthop Res: Off Publ Orthop Res Soc* 8(5):662–670. <https://doi.org/10.1002/jor.1100080507>
5. Coelho PG, Fernandes PR, Rodrigues HC, Cardoso JB, Guedes JM (2009) Numerical modeling of bone tissue adaptation—a hierarchical approach for bone apparent density and trabecular structure. *J Biomech* 42(7):830–837. <https://doi.org/10.1016/j.jbiomech.2009.01.020>
6. Pivonka P, Buenzli PR, Scheiner S, Hellmich C, Dunstan CR (2013) The influence of bone surface availability in bone remodelling—a mathematical model including coupled geometrical and biomechanical regulations of bone cells. *Eng Struct* 47:134–147. <https://doi.org/10.1016/j.engstruct.2012.09.006>
7. Turner AW, Gillies RM, Sekel R, Morris P, Bruce W, Walsh WR (2005) Computational bone remodelling simulations and comparisons with DEXA results. *J Orthopaed Res : Off Publ Orthop Res Soc* 23(4):705–712. <https://doi.org/10.1016/j.orthres.2005.02.002>
8. Hambli R, Katerchi H, Benhamou CL (2011) Multiscale methodology for bone remodelling simulation using coupled finite element and neural network computation. *Biomech Model Mechanobiol* 10(1):133–145. <https://doi.org/10.1007/s10237-010-0222-x>
9. White AA, Panjabi MM (1990) *Clinical biomechanics of the spine*, 2nd edn. Lippincott, Philadelphia
10. Wang X, Thomas CD, Clement JG, Das R, Davies H, Fernandez JW (2015) A mechanostatistical approach to cortical bone remodelling: an equine model. *Biomech Model Mechanobiol* 15(1):29–42. <https://doi.org/10.1007/s10237-015-0669-x>
11. Ackerman MJ, Spitzer VM, Scherzinger AL, Whitlock DG (1995) The Visible Human data set: an image resource for anatomical visualization. *Medinfo. MEDINFO* 8(Pt 2):1195–1198
12. Bell KL, Loveridge N, Power J, Garrahan N, Meggitt BF, Reeve J (1999) Regional differences in cortical porosity in the fractured femoral neck. *Bone* 24(1):57–64

13. Sartori M, Reggiani M, Lloyd DG, Pagello E (2011) A neuromusculoskeletal model of the human lower limb: towards EMG-driven actuation of multiple joints in powered orthoses. In: IEEE international conference on rehabilitation robotics [proceedings] 2011, 5975441 (2011). <https://doi.org/10.1109/icorr.2011.5975441>
14. Gray H (1918) *Anatomy of the human body*, 20th edn. Lea & Febiger, Philadelphia
15. Shinohara M, Sabra K, Gennisson JL, Fink M, Tanter M (2010) Real-time visualization of muscle stiffness distribution with ultrasound shear wave imaging during muscle contraction. *Muscle Nerve* 42(3):438–441. <https://doi.org/10.1002/mus.21723>
16. Herzog W (2000) *Skeletal muscle mechanics: from mechanisms to function*. Wiley, Chichester
17. Smit TH, Huyghe JM, Cowin SC (2002) Estimation of the poroelastic parameters of cortical bone. *J Biomech* 35(6):829–835
18. Hayes WC, Keer LM, Herrmann G, Mockros LF (1972) A mathematical analysis for indentation tests of articular cartilage. *J Biomech* 5(5):541–551
19. Brown TD, Ferguson AB Jr (1980) Mechanical property distributions in the cancellous bone of the human proximal femur. *Acta Orthop Scand* 51(3):429–437
20. U.S. FDA Cellular Tissue and Gene Therapies Advisory Committee: Meeting #38 (2005) Cellular products for joint surface repair briefing document. In: U.S. Food and Drug Administration (ed) Rockville, MD
21. Keller TS, Mao Z, Spengler DM (1990) Young's modulus, bending strength, and tissue physical properties of human compact bone. *J Orthopaed Res Off Publ Orthopaed Res Soc* 8(4):592–603. <https://doi.org/10.1002/jor.1100080416>
22. Lee WR (1964) Appositional bone formation in canine bone: a quantitative microscopic study using tetracycline markers. *J Anat* 98:665–677
23. Davies HMS (1995) *The adaptive response of the equine metacarpus to locomotory stress*. PhD Thesis, University of Melbourne
24. Wold S, Sjostrom M, Eriksson L (2001) PLS-regression: a basic tool of chemometrics. *Chemometr Intell Lab* 58(2):109–130. [https://doi.org/10.1016/S0169-7439\(01\)00155-1](https://doi.org/10.1016/S0169-7439(01)00155-1)
25. Martelli S (2017) Femoral neck strain during maximal contraction of isolated hip-spanning muscle groups. *Comput Math Method Med* 2017:2873789. <https://doi.org/10.1155/2017/2873789>